Altmann, J. B., Müller, B., Müller, T., Heidbach, O., Tingay, M., Weißhardt, A. (2014): Pore pressure stress coupling in 3D and consequences for reservoir stress states and fault reactivation. - *Geothermics*, *52*, p. 195-205.

DOI: http://doi.org/10.1016/j.geothermics.2014.01.004

Geothermics 52 (2014) 195-205

Pore pressure stress coupling in 3D and consequences for reservoir stress states and fault reactivation

J.B. Altmann[a], B.I.R. Müller[b], T.M. Müller[c], O. Heidbach[a,*], M.R.P. Tingay[d], A. Weißhardt[e]

[a] *Helmholtz Centre Potsdam, GFZ German Research Centre for Geosciences, Potsdam, Germany*
[b] *Geothermal Research Centre of the State of Baden-Württemberg (LFZG), Karlsruhe, Germany*
[c] *CSIRO, Australian Resources Research Centre, Kensington, Australia*
[d] *Australian School of Petroleum Science, The University of Adelaide, Adelaide, Australia*
[e] *ITASCA Consultants GmbH, Gelsenkirchen, Germany*

ARTICLE INFO

Article history:
Received 6 January 2013
Received in revised form 14 September 2013
Accepted 8 January 2014
Available online 30 January 2014

Keywords:
Geomechanics
Reservoir geophysics
Stress regime
Pore pressure

ABSTRACT

The spatio-temporal changes of the stress state in a geothermal reservoir are of key importance for the understanding of induced seismicity and planning of injection and depletion strategies. In particular the poro-elastic effects on the stress state due to re-injection or depletion of water are of interest for both geothermal projects and hydrocarbon exploitation. In addition to the conventionally used effective stress concept, poro-elasticity affects the stress tensor components differently as a function of changes in pore pressure. Here, we provide an analytical base for the long-term changes of the 3D stress tensor components as a function of pore pressure changes. Results indicate that for a constant rate of injection or depletion the coupling between pore pressure and all stress tensor components depends on the location in the reservoir with respect to the re-injection/depletion point as well as the time since the beginning of pore pressure changes. Our systematic analysis suggests that poro-elastic stress changes can even locally modify the given tectonic stress regime. Furthermore, the results predict that localized changes of maximum shear stress can lead to different fracture orientations than those expected when poro-elastic effects are not considered. These results indicate a need for 3D geomechanical-numerical studies of more realistic reservoir settings in order to study the 3D effects of pore pressure/stress coupling. Our generic 3D geomechanical-numerical study shows that less than two years of production of a single well changes shear stresses by 0.2 MPa. Thus, in reservoirs with decades of production shear stress change can reach sufficiently high values to re-activate pre-existing faults or even generate new fractures with unexpected orientations.

1. Introduction

Induced seismicity in geothermal reservoirs is generated by changes in pore pressure during stimulation experiments, reservoir production time, and re-injection of water (e.g. *Evans et al.*, 2012; *Majer et al.*, 2007; *Suckale*, 2010). In long-term producing georeservoirs, such as the geothermal field The Geysers in California or the gas field Lacq in south western France, the reservoir pressure declines steadily (*Goyal and Conant*, 2010; *Segall et al.*, 1994). To maintain the reservoir pressure, massive injection of waste water has been conducted for more than a decade at The Geysers geothermal field with significant pore pressure changes, particularly near the re-injection wells (*Rutqvist et al.*, 2013). With time, pore pressure changes diffuse throughout the reservoir and are thus a function of time and distance to the injection or production well. These spatio-temporal changes in reservoir pressures lead to changes in stress and deformation of the reservoir and the surrounding rocks (*Mossop and Segall*, 1997; *Zoback*, 2010). Pore pressure counteracts the external stresses acting on the rock matrix, which prompted *Terzaghi* (1943) to propose the effective stress concept; he defined effective stresses as the difference between the total stress and the pore pressure. However, measurements in hydrocarbon reservoirs have revealed that the total minimum horizontal stress changes ΔS_h in response to changes in pore pressure ΔP result in a $\Delta S_h/\Delta P$ ratio of 0.64 (*Addis*, 1997; *Hillis*, 2000).

According to *Goulty* (2003) this observation can be ascribed to three different mechanisms: (1) normal compaction of the reservoir due to depletion. Sediments undergo normal compaction and reduction in porosity when the mean effective stress increases. Then, the $\Delta S_h/\Delta P$ ratio for sediments compacted under zero horizontal strain conditions and no changes of vertical stress can be derived using the coefficient of earth pressure K_0. (2) Normal faulting based on the assumption that critically stressed faults in a normal faulting regime are always present and (3) poro-elastic effects. The relation of these stress changing mechanisms to induced seismicity is demonstrated by *Hillis* (2001). Production induced seismicity has been found worldwide in oil and gas fields (*Maxwell and Urbancic*, 2001; *Suckale*, 2010). Injection related seismicity is frequently associated with stimulation in geothermal wells (*Cuenot et al.*, 2006) or CO_2 sequestration and has been successfully interpreted using the pore pressure diffusion equation (*Shapiro et al.*, 1998, 2003) or the spatio-temporal evolution of stress and pore pressure (*Rozhko*, 2010; *Schoenball et al.*, 2010). *Hillis* (2000) and *Tingay et al.* (2003) call the phenomenon of the observed $\Delta S_h/\Delta P$ ratio changes 'pore pressure/stress coupling'. All three mechanisms cited above can contribute to the $\Delta S_h/\Delta P$ ratio, but in this paper we focus on the poro-elastic contributions.

To date the estimation of $\Delta S_h/\Delta P$ ratios has been performed with models with one or several of the following assumptions (e.g. *Engelder and Fischer*, 1994; *Segall*, 1992; *Hettema et al.*,

* Corresponding author. Tel.: +49 331 288 2814; fax: +49 331 288 1127.
E-mail address: heidbach@gfz-potsdam.de (O. Heidbach)

1998; *Segall and Fitzgerald*, 1998): uniaxial vertical strain, uniform or prescribed pore pressure change within the reservoir, ring pore pressure sources, horizontally layered reservoirs and laterally constant vertical stress. With these assumptions - in particular the implicit homogeneous pore pressure reduction within the reservoir or zero lateral strain boundary conditions - the models are not capable to investigate the 3D effects of pore pressure stress coupling; furthermore these assumptions are rather inappropriate for producing fields. The limitations of these assumptions are best displayed e.g. by time-lapse investigations (*Sayers*, 2004, 2006) in combination with geomechanical modelling (e.g. *Herwanger and Horne*, 2005; *Schutjens et al.*, 2010; *Settari and Sen*, 2007; *Rutqvist et al.*, 2008). They reveal that the impact of pore pressure changes not only affects S_h, but all components of the stress tensor, which should be considered for all stress-dependent field operations such as directional drilling, stimulation, placement of infill wells etc. For this reason the full 3D poro-elastic equations should be incorporated in geomechanical-numerical models.

The key objective of our paper is to systematically investigate the three-dimensional impact of pore pressure/stress coupling on the stress tensor components. In particular we quantitatively assess the injection phase using the analytical solutions of *Rudnicki* (1986) and *Altmann et al.* (2010) in the long-term limit for a point source (injection or depletion) in a homogenous, isotropic, poro-elastic infinite medium. This approach is not restricted by the assumptions of a normal faulting stress regime, constant vertical stress S_V and horizontal layering. In particular it can be applied to: (1) different tectonic settings, such as thrust and normal faulting (where S_V is the least or the maximum principal stress, respectively) or strike slip (S_V is the intermediate principal stress) regimes. (2) Studying the effects of localized pore pressure changes. (3) Providing estimates of the $\Delta S_h/\Delta P$ ratios for all components of the principal stress tensor, not only for S_h.

We present pore pressure induced stress magnitude and stress orientation changes in the long term limit using a constant fluid injection/production rate. Major findings of our study are that pore pressure/stress coupling can lead to changes in induced fracture orientations, change in fracture closure pressure (and therefore create problems in wellbore stability), and localized changes of stress magnitudes that can result in an alteration of the tectonic stress regime (in particular when pore pressure changes exceed the maximum shear stresses before injection or depletion).

2. Basic relations between pore pressure and stress

Terzaghi (1943) showed that the strength of fully saturated soils and rocks is controlled by the effective stress S_{eff} according to

$$S_{eff} = S - P \tag{1}$$

Eq. (1) governs the pressure dependence where P is the pore pressure and S the total stress: the amount of pore pressure change determines the change of effective stress. This concept is successful in explaining seismicity associated with injection into reservoirs, e.g. for secondary production methods or enhanced geothermal systems (*Deichmann and Evans*, 2007; *Valley and Evans*, 2007). According to *Coulomb* (1773) pre-existing faults are reactivated when the shear stress τ exceeds:

$$|\tau| \geq C + \mu \cdot S_{n_{eff}} \tag{2}$$

with C as cohesion, μ as coefficient of static friction of the fault and $S_{n,eff}$ as effective normal stress on the fault (compression defined positive). According to Eqs. (1) and (2), an increase of pore pressure resulting from injection leads to a reduction of $S_{n,eff}$ on the pre-existing fault. This modifies the state of stress such that the fault is more likely to fail. This can be visualized by shifting the Mohr circle in the Mohr diagram to smaller effective stresses (Fig. 1a). Vice versa, production from a reservoir diminishes the pore pressure and reduces the likelihood of fault reactivation. Therefore, this concept cannot readily explain production-induced seismicity within reservoirs.

Biot (1962) refined the effective stress concept of *Terzaghi* (1943) by introducing the effective stress coefficient for the bulk volume or Biot–Willis coefficient α. For saturated porous rock material the effective stress responsible for rock deformation is:

$$S_{eff} = S - \alpha \cdot P \tag{3}$$

Frequently α is assumed to be 1, which reduces Eq. (3) to Eq. (1). However, there is evidence that the Biot–Willis coefficient may be as low as 0.5 in compacted shales (see compilations in *Jaeger et al.*, 2007 or *Sarker and Batzle*, 2008). In the case of partial saturation, the effective stress depends on the combination of fluid pressure in the wetting and the non-wetting fluid phase (*Bishop*, 1959), but this is not within the scope of this paper.

According to Eq. (3) (Fig. 1) effective stresses can change due to three effects. (a) Directly with variations in pore pressure P (Fig. 1a). (b) Changes in Biot–Willis coefficient α due to pore pressure changes (Fig. 1b); this can occur when changes in pore pressure affect the pore volume of the reservoir rock (porosity), thus changing α. If the Biot–Willis coefficient experiences anisotropic changes (*Braun*, 2007), the effective stress components are affected differently and α has to be replaced by α_{ij}. (c) Pore pressure changes can induce changes in the stress state which is called pore pressure/stress coupling (PSC). The abbreviation PSC was introduced by *Altmann et al.* (2010) for the coupling between minimum horizontal stress S_h and pore pressure P, but in this paper it is used in a more general sense, namely for coupling between pore pressure and the stress components in 3D. PSC results from introducing the effective stress principle in the constitutive equations and combining it with the pressure diffusion equation. This leads to a coupling of pore pressure and total stress, so that the pore pressure does not only affect the effective stress but also the total stress (Fig. 1c).

Assuming equal horizontal stresses ($S_h = S_H$, S_h minimum horizontal stress, S_H maximum horizontal stress), constant vertical stress S_V and no horizontal strains, *Engelder and Fischer* (1994) and others (e.g. *Addis*, 1997; *Hillis*, 2000) present the following relationship

$$\frac{\Delta S_h}{\Delta P} = \alpha \frac{1-2\nu}{1-\nu} \tag{4}$$

where ΔP is the change in pore pressure. For $\alpha = 1$ and a Poisson's ratio of $\nu = 0.25$ this results in $\Delta S_h/\Delta P = 0.67$; for $\alpha = 1$ and $\nu = 0.2$, the coupling coefficient is 0.75. These values are within the range of values derived from repeated measurements of pore pressure and minimum horizontal stress in numerous reservoirs (*Engelder and Fischer*, 1994; *Addis*, 1997).

In contrast to the Terzaghi approach, the PSC concept of *Engelder and Fischer* (1994) also explains seismicity during reservoir depletion: reduction of pore pressure changes the effective vertical stress($S_{Veff} = S_V - P$) by ΔP because S_V is assumed to remain constant with pressure changes. The effective minimum horizontal stress changes differently, namely by

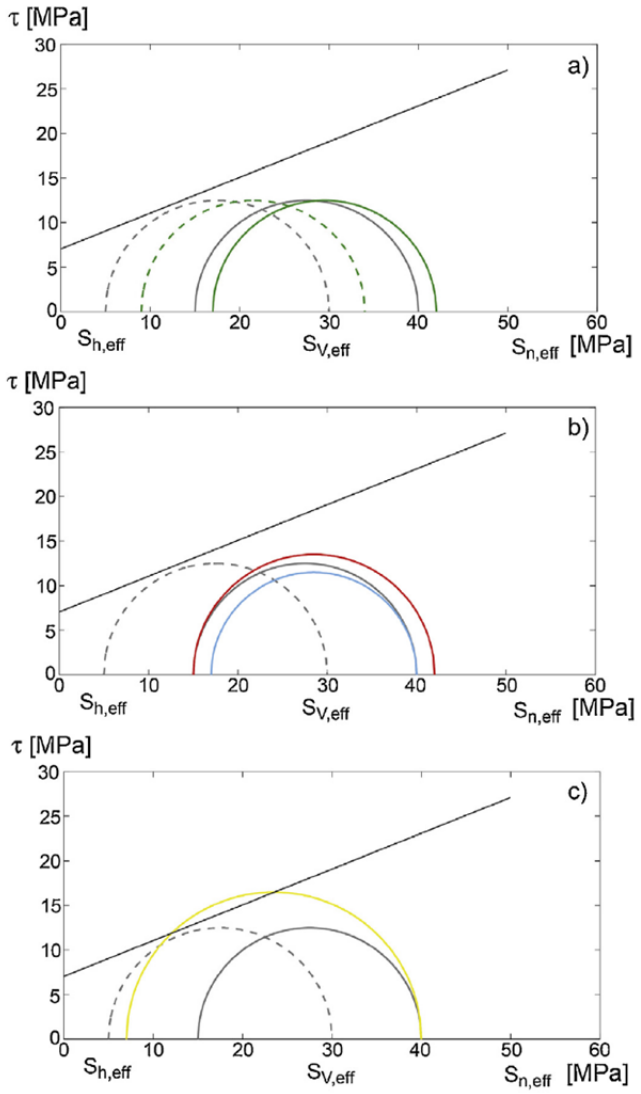

Figure 1. Effects of pore pressure on effective stresses. The dashed grey circles represent the state of effective stress before production from a reservoir if the Biot–Willis coefficient is assumed to be 1.0. The density of the overburden is ca. 2500 kg/m³ and the depth of the reservoir approximately 2 km. Production reduces the initial pore pressure by $\Delta P = 10$ MPa (solid grey circles). (a) Terzaghi approach: the effective stress changes by the amount of pore pressure change without change in maximum shear stress (Eq. (3)) The solid grey Mohr circle indicates the state of effective stress after production under the assumption of Terzaghi' principle. The green Mohr circles indicate the states of effective stress before (dashed circle) and after (solid circle) production when $\alpha = 0.8$. (b) For anisotropic changes of the Biot–Willis coefficient, the size of the Mohr circle increases if the change of α in the direction of the larger principal stress is larger (for example from $\alpha = 1.0$ to $\alpha = 0.6$) than in orientation of the minimum principal stress (e.g. change from $\alpha = 1.0$ to $\alpha = 0.8$, red Mohr circle). If the change of α in the orientation of the minimum horizontal stress is larger than in the orientation of the maximum principal stress, the size of the Mohr circle decreases (blue curve). (c) With change in total stress. Here, the changes are due to poro-elastic pore pressure/stress coupling according to *Engelder and Fischer* (1994), where the effective horizontal stress changes during depletion while the vertical stress remains constant (yellow circle). A coupling coefficient of 0.8 for the minimum horizontal stress S_h is assumed. (For interpretation of the references to colour in this figure legend, the reader is referred to the web version of the article.)

$\Delta P + \Delta S_h$ (note ΔP and ΔS_h are both negative for production). This leads to an increase in the differential stress (defined as difference between the maximum and minimum principal stress) which can lead to failure. Fig. 1c illustrates the PSC approach according to *Engelder and Fischer* (1994) and *Hillis* (2000, 2001), using Mohr' Circles to present conditions before and after depletion. The reduction of pore pressure decreases S_h, and thus causes higher differential stress (for S_V assumed to be constant), which could lead to fault reactivation. However, these considerations have their limitation because the assumptions used to derive Eq. (4) apply only to a normal faulting stress state ($S_V > S_H > S_h$) and horizontally infinite reservoirs. Furthermore, it does not include the spatial distribution of pore pressure changes due to extraction of fluids at wells.

3. Tensor character of the spatio-temporal evolution of pore pressure and total stress components

To assess the impact of pore pressure changes on the stress tensor in 3D we consider the case of a homogeneous saturated poro-elastic medium and use the Eqs. (25) and (26) of *Rudnicki* (1986), who provides the changes of stress and pore pressure distribution for continuous fluid injection ($q > 0$) or depletion ($q < 0$) at a point source:

$$\Delta P(\mathbf{x}, t) = \frac{q}{\rho_f c}\frac{1}{4\pi r}\left[\frac{(\lambda_u - \lambda)(\lambda + 2G)}{\alpha^2(\lambda_u + 2G)}\right]\mathrm{erfc}\left(\frac{1}{2}\xi\right) \tag{5}$$

$$\begin{aligned}\Delta S_{ij}(\mathbf{x}, t) &= -\frac{q}{\rho_f c}\frac{(\lambda_u - \lambda)G}{4\pi r\alpha(\lambda_u + 2G)}\left\{\delta_{ij}\left[\mathrm{erfc}\left(\frac{1}{2}\xi\right) - \frac{2}{\xi^2}g(\xi)\right]\right. \\ &\left. + \frac{x_i x_j}{r^2}\left[\mathrm{erfc}\left(\frac{1}{2}\xi\right) + \frac{6}{\xi^2}g(\xi)\right]\right\}\end{aligned} \tag{6}$$

where q represents a constant-rate fluid mass source and ρ_f the fluid density, $\xi = r/\sqrt{ct}$ is the Boltzmann variable and c the hydraulic diffusivity of the rock. The drained and undrained Lamé parameters are λ and λ_u, G is the shear modulus and α is defined as $\alpha = 1 - (K/K_g)$ with the bulk modulus K and the bulk modulus of the solid constituents K_g. The function $\mathrm{erfc}(z)$ is the complementary error function of variable z and is connected to the error function $\mathrm{erfc}(z)$ by $\mathrm{erfc}(z) = 1 - \mathrm{erfc}(z)$, and the vector between pressure source (for injection $q > 0$, for depletion $q < 0$) and observation point is x, r its vector length. In Eq. (6) the function

$$\begin{aligned}g(\xi) &= \frac{1}{2\sqrt{\pi}}\int_0^{\xi} s^2 \exp\left(-\frac{1}{4}s^2\right) ds \\ &= \mathrm{erf}\left(\frac{1}{2}\xi\right) - \frac{1}{\sqrt{\pi}}\xi\exp\left(-\frac{1}{4}\xi^2\right)\end{aligned} \tag{7}$$

is used. *Rudnicki* (1986) defines the diffusivity c as

$$c = \frac{\kappa \cdot (\lambda_u - \lambda) \cdot (\lambda - 2\mu)}{\alpha^2(\lambda_u + 2\mu)} \tag{8}$$

with $\kappa = k/\gamma$, where k is the permeability in units of m² and γ is the dynamic fluid viscosity in units of Pa s.

From Eqs. (5) and (6) it is obvious that the changes of pore pressure and stress are functions of distance to the injection point, duration of injection, injection rate and permeability (assuming that the γ and the elastic properties are homogeneous). By dividing Eq. (6) by Eq. (5) we obtain the pore pressure/stress coupling ratio $\Delta S_{ij}/\Delta P$) for the components of the stress tensor. For a detailed derivation of the equations we refer

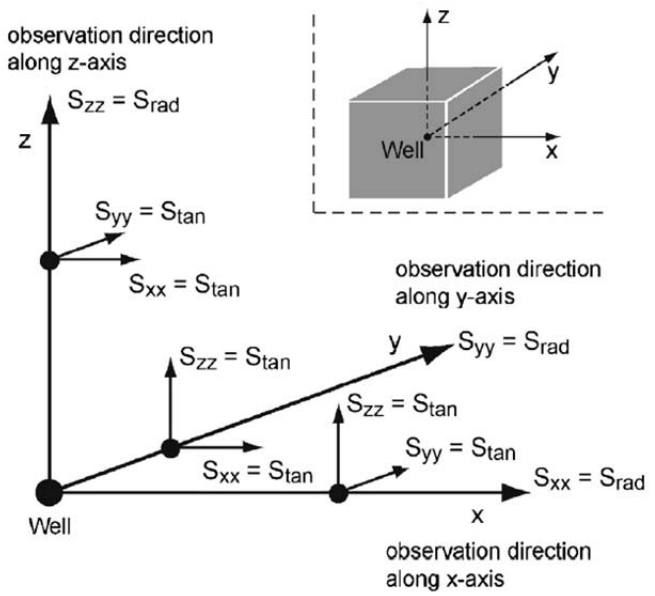

Figure 2. Illustration of the different stress components with respect to the injection/depletion point and co-ordinate axes.

to *Altmann et al.* (2010) and *Wang* (2000).

Due to the radial symmetry we consider the radial and tangential stress components with respect to the injection (depletion) point (Fig. 2). For example, in case of injection at the origin of the coordinate system, the stress S_{xx} is a radial stress for all positions along the x-axis, but a tangential stress for all positions along the y-axis. ΔS_{rad} denotes the change of the radial stress component and ΔS_{tan} denotes the change of the tangential stress component. Fig. 3 shows the radial and tangential stress changes for a particular representative case as a function of time since the beginning of injection at a fixed position (here 200 m distance to the injection point). There are considerable differences in radial and tangential stress changes created by the same pore pressure change. ΔS_{rad} is larger than ΔS_{tan} and only after the first 21 days after injection initiation does ΔP exceed ΔS_{rad}. This can be interpreted as indicating that the stress is transferred poro-elastically faster than the pore pressure diffuses through the medium. In the same time interval ΔS_{tan} is negative. For the parameters chosen (permeability of $k = 10^{-15}$ m², $\alpha = 0.65$, $\lambda = 8.4$ GPa, $\lambda_u = 11.2$ GPa, $\mu = 8.4$ GPa and $\nu = 0.25$) the long-term limit at a distance of 200 m is reached after approximately three years of constant injection, when radial and tangential stresses do not change anymore (Fig. 3).

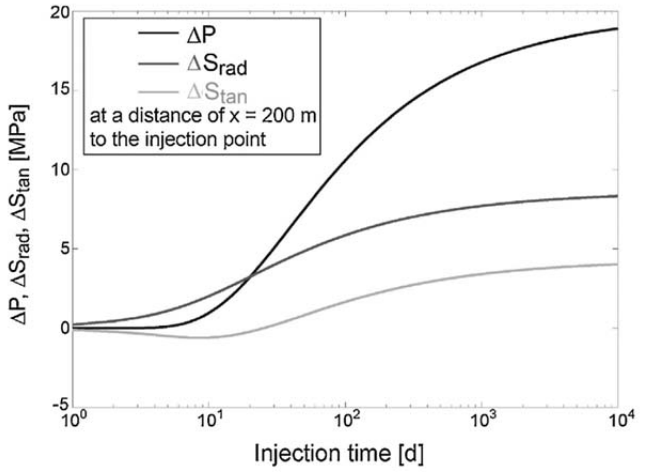

Figure 3. Example for pore pressure and stress change calculated according to *Rudnicki* (1986) for injection into full space at 50 l/s into a medium with a permeability of $k = 10^{-15}$ m², $\alpha = 0.65$, $\lambda = 8.4$ GPa, $\lambda_u = 11.2$ GPa, $\mu = 8.4$ GPa and $\nu = 0.25$. The values are calculated at a location 200 m from the injection point as a function of injection time. Note, that radial and tangential stresses are different in magnitude.

As shown in Fig. 3 changes in pore pressure create significantly different changes in radial and tangential stress components. In this paper we focus on the long-term limit of stress changes. These long-term ($t \to \infty$) limits of radial and tangential stress changes can be derived from Eqs. (5) and (6) as shown by *Altmann et al.* (2010)

$$\lim_{t\to\infty} \frac{\Delta S_{rad}(r,t)}{\Delta P(r,t)} = \alpha \frac{1-2\nu}{1-\nu} \tag{9a}$$

$$\lim_{t\to\infty} \frac{\Delta S_{tan}(r,t)}{\Delta P(r,t)} = \frac{1}{2}\alpha \frac{1-2\nu}{1-\nu} \tag{9b}$$

In the long-term limit, the total principal stress tensor after a pore pressure change P becomes:

$$S_{ij} = \begin{bmatrix} S_{rad} + \alpha\frac{1-2\nu}{1-\nu}\Delta P & 0 & 0 \\ 0 & \Delta S_{tan} + \frac{1}{2}\alpha\frac{1-2\nu}{1-\nu}\Delta P & 0 \\ 0 & 0 & \Delta S_{tan} + \frac{1}{2}\alpha\frac{1-2\nu}{1-\nu}\Delta P \end{bmatrix} \tag{10}$$

Under the assumption of a Poisson' ratio of 0.25 and a Biot–Willis coefficient of 1, the stress tensor after the application of a pressure change of P becomes

$$S_{ij} = \begin{bmatrix} S_{rad} + \frac{2}{3}\Delta P & 0 & 0 \\ 0 & S_{tan} + \frac{1}{3}\Delta P & 0 \\ 0 & 0 & S_{tan} + \frac{1}{3}\Delta P \end{bmatrix} \tag{11}$$

The corresponding effective stresses become:

$$S_{ij_{eff}} = \begin{bmatrix} S_{rad} - \frac{1}{3}\Delta P & 0 & 0 \\ 0 & S_{tan} + \frac{2}{3}\Delta P & 0 \\ 0 & 0 & S_{tan} + \frac{2}{3}\Delta P \end{bmatrix} \tag{12}$$

4. PSC for reservoirs in different tectonic stress regimes

In this section we investigate the changes in effective stress due to pore pressure changes in saturated reservoirs. In particular we systematically investigate the impact of different tectonic stress regimes and different initial differential stresses. The pore pressures we are using for these scenarios are in the range of measured values in reservoirs; for example, 45 MPa reduction in Ekofisk (*Teufel et al.*, 1991) and the Lacq field (*Grasso and Wittlinger*, 1990), 10 MPa in the Imogene field and ca. 28 MPa in Fashing gas field (*Pennington et al.*, 1986).

Using the PSC concept in 3D based on the Rudnicki's analytical solution for a constant point source embedded in an isotropic homogeneous medium (Eqs. (11) and (12)), the increase in effective stress due to a 30 MPa pore pressure reduction is 10

Table 1
Relative stress magnitudes for different tectonic stress regimes.

Regime	Relative stress magnitudes	Differential stress $\sigma_1 - \sigma_3$
NF: Normal Faulting regime	$S_V > S_H > S_h$	$S_V - S_H$
SS: Strike Slip Faulting regime	$S_H > S_V > S_h$	$S_H > S_h$
TF: Thrust Faulting regime	$S_H > S_h > S_V$	$S_H > S_V$

MPa, for the radial stress and 20 MPa for the tangential stresses. This results in decreases in differential stress of up to 10 MPa depending on the tectonic stress regime and the position within the reservoir. Such changes in differential stress are quite significant at shallow reservoir depths. To infer the consequences of PSC and associated changes of differential stresses for reservoir depletion/injection, we estimate the stress state of the long-term injection (depletion) limit for the three different tectonic stress regimes, normal faulting, strike slip and thrust faulting regime (Table 1).

4.1. Hypothetical reservoir model

In the following, we consider a hypothetical reservoir (Fig. 4). Herein we deduce the stress changes for long production/injection intervals due to pore pressure variations at three positions along the principal stress axes at equal distance R to the injection (depletion) point P. Due to the radial symmetry it does not matter whether the points are located in the positive or negative axis direction. For each of the tectonic stress regimes, the total vertical stress is assumed to be given by the weight of the overburden of the reservoir and the initial pore pressure is considered to be hydrostatic. Thus, the initial vertical effective stress is 50 MPa, which corresponds to a depth of approximately 3000 m for a mass density of 2700 kg/m^3 and hydrostatic pore pressure of 30 MPa at that depth. In order to represent different tectonic stress regimes, the magnitudes of S_h and S_H are varied with respect to the magnitude of S_V. These different initial stress states (before production or injection) are used to calculate stress changes in different tectonic stress regimes and at different locations with respect to the injection or production point. In Tables 2 and 3 pore pressure and stress changes, as well as stress states before and after injection and production, are listed.

Fig. 5 displays the effective stress states of points A, B and C using Mohr circles. Black dashed line Mohr circles indicate initial effective stress states before depletion or injection. The states of stress at points A, B, C after depletion or injection are given in blue, red and green colours. For comparison, the grey solid line Mohr circles show the stress states at A, B, C assuming no coupling between total stress and pore pressure, after *Terzaghi* (1943).

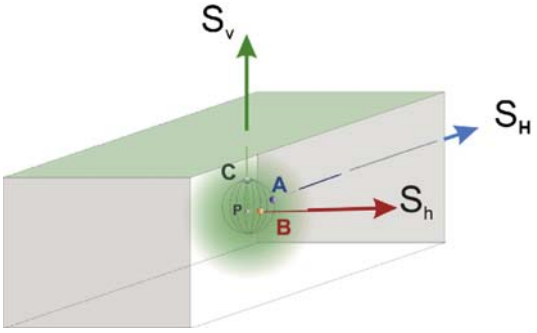

Figure 4. Sketch to explain the positions of points A, B, C which are located at an equal distance to the injection point along the axes of the principal stresses S_H, S_h, S_V. The shaded area represents the pore pressure changes around the injection (depletion) point P which is located at the origin of the co-ordinate system.

With PSC the size of the Mohr circles, which represents the differential stress, is either reduced or enlarged relative to those calculated without consideration of changes in total stress (solid line grey Mohr circles in Fig. 5). In considering different tectonic stress regimes we assume a horizontally and vertically homogeneous regional stress field and thus can superimpose the stress pattern of radial and tangential stresses of the injection/depletion. According to Eq. (12) the radial stress components change due to injection/depletion by $2/3\ \Delta P$ whereas the tangential components change by $1/3\ \Delta P$. This also changes the effective stresses, namely by $-1/3\ \Delta P$ in radial direction and by $-2/3\ \Delta P$ in tangential directions. Along the S_h axis, the additional stress component due to injection/depletion, which acts parallel to S_h, is a radial stress, the stresses in the vertical direction and parallel to S_H are tangential stresses. Along the orientation of S_V, the injection/depletion related stress components parallel to S_h and S_H are tangential components, and the stress in vertical direction is a radial stress. Parallel to the orientation of S_H, the additional vertical stress components and those parallel to S_h are tangential components and the additional compo-

Table 2
Effective stresses before injection, pore pressure change due to injection, total stress changes caused by injection, effective stress changes caused by injection, and effective stresses after injection, all at three different locations with respect to the injection point for three different tectonic stress regimes. All values are given in MPa.

Point	NF-regime			SS-regime			TF-regime		
	A	B	C	A	B	C	A	B	C
$S_{V_{eff,ini}}$	50	50	50	50	50	50	50	50	50
$S_{H_{eff,ini}}$	40	40	40	65	65	65	65	65	65
$S_{h_{eff,ini}}$	25	25	25	25	25	25	55	55	55
ΔP	15	15	15	15	15	15	15	15	15
$\Delta S_{V_{tot}}$	4.5	4.5	9	4.5	4.5	9	4.5	4.5	9
$\Delta S_{H_{tot}}$	9	4.5	4.5	9	4.5	4.5	9	4.5	4.5
$\Delta S_{h_{tot}}$	4.5	9	4.5	4.5	9	4.5	4.5	9	4.5
$\Delta S_{V_{eff}}$	−10.5	−10.5	−6	−10.5	−10.5	−6	−10.5	−10.5	−6
$\Delta S_{H_{eff}}$	−6	−10.5	−10.5	−6	−10.5	−10.5	−6	−10.5	−10.5
$\Delta S_{h_{eff}}$	−10.5	−6	−10.5	−10.5	−6	−10.5	−10.5	−6	−10.5
$S_{V_{eff}}$	39.5	39.5	44	39.5	39.5	44	39.5	39.5	44
$S_{H_{eff}}$	34	29.5	29.5	59	54.5	54.5	59	54.5	54.5
$S_{h_{eff}}$	14.5	19	14.5	14.5	19	14.5	44.5	49	44.5

Table 3
Effective stresses before production, pore pressure change due to production, total stress changes caused by production, effective stress changes caused by production, and effective stresses after production, all at three different locations with respect to the production point for three different tectonic stress regimes. All values are given in MPa.

Point	NF-regime			SS-regime			TF-regime		
	A	B	C	A	B	C	A	B	C
$S_{V_{eff,ini}}$	50	50	50	50	50	50	50	50	50
$S_{H_{eff,ini}}$	40	40	40	65	65	65	65	65	65
$S_{h_{eff,ini}}$	25	25	25	25	25	25	55	55	55
ΔP	−15	−15	−15	−15	−15	−15	−15	−15	−15
$\Delta S_{V_{tot}}$	−4.5	−4.5	−9	−4.5	−4.5	−9	−4.5	−4.5	−9
$\Delta S_{H_{tot}}$	−9	−4.5	−4.5	−9	−4.5	−4.5	−9	−4.5	−4.5
$\Delta S_{h_{tot}}$	−4.5	−9	−4.5	−4.5	−9	−4.5	−4.5	−9	−4.5
$\Delta S_{V_{eff}}$	10.5	10.5	6	10.5	10.5	6	10.5	10.5	6
$\Delta S_{H_{eff}}$	6	10.5	10.5	6	10.5	10.5	6	10.5	10.5
$\Delta S_{h_{eff}}$	10.5	6	10.5	10.5	6	10.5	10.5	6	10.5
$S_{V_{eff}}$	60.5	60.5	56	60.5	60.5	56	60.5	60.5	56
$S_{H_{eff}}$	46	50.5	50.5	71	75.5	75.5	71	75.5	75.5
$S_{h_{eff}}$	35.5	31	35.5	35.5	31	35.5	65.5	61	65.5

nent parallel to S_H is the radial component. Depending on the background stress pattern (the tectonic stress regime) the maximum shear stress changes differently.

4.2. Normal faulting regime

In the normal faulting regime the differential stress is determined by S_V and S_h. In the event of depletion, the pore pressure along the S_h orientation increases the effective minimum stress by $|1/3\,\Delta P|$ because the minimum horizontal stress is a radial component, whereas the effective vertical stress is a tangential component and thus increased by $|2/3\,\Delta P|$. Therefore the reduction of pore pressure leads to an increase of differential stress at position B (red Mohr circle). Similarly, a reduction of pore pressure leads to a reduction of differential stress at point C (green Mohr circle). No change occurs along the S_H orientation and thus at point A (blue Mohr circle). The maximum increase of shear stress during depletion occurs parallel to S_h.

In the case of injection, the effective vertical stress at point C reduces by $1/3\,\Delta P$, whereas the effective horizontal stresses both reduce by $2/3\,\Delta P$. This leads to greater differential stresses at point C on the S_V-axis. At position A, the effective vertical

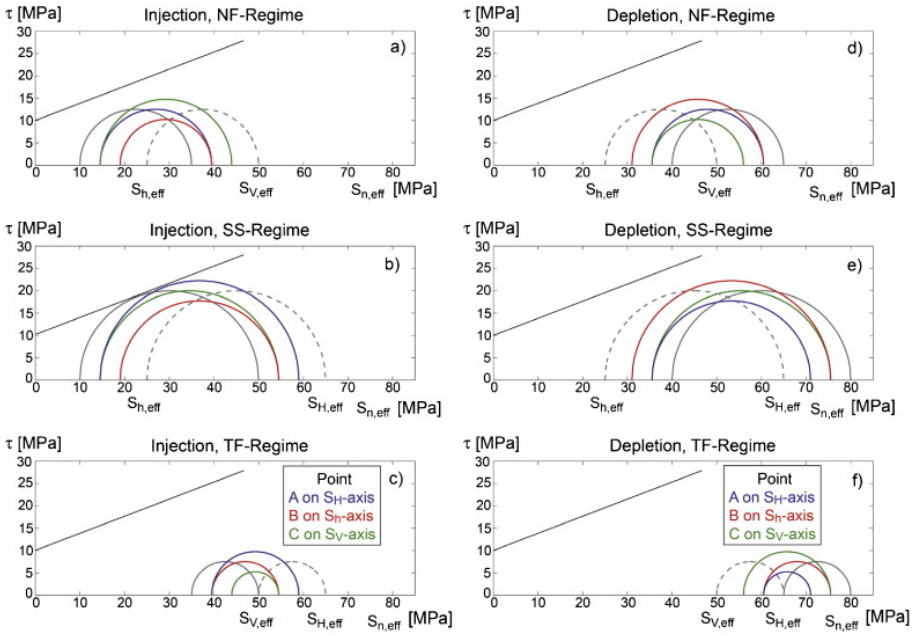

Figure 5. Effective stress states at positions A, B, C for depletion and injection in normal faulting (NF), strike slip (SS) and thrust faulting (TF) regimes. The stress states are displayed as Mohr circles with $S_{n_{eff}}$ as effective normal stress and τ as shear stress. Grey dashed circles denote the initial effective stress conditions, with the intermediate principal stress assumed to be roughly halfway in between the maximum and the minimum principal stresses. Grey solid circles denote the classical Terzaghi effective stress condition after pore pressure reduction in the case of depletion or pore pressure increase in the case of injection. Without pore pressure/stress coupling the size of the Mohr circle remains constant and its position is shifted to the right in case of depletion and to the left in case of injection. With pore pressure/stress coupling, the differential stress changes. Red circles are stress states along the S_h axis, blue circles are stress states along the S_H axis and green circles are stress states along the S_V axis. The hypothetical failure envelope (solid straight line) is characterized by a relatively high cohesion of 10 MPa and a coefficient of static friction of $\mu = 0.6$. (For interpretation of the references to colour in this figure legend, the reader is referred to the web version of the article.)

Table 4
Localized change of tectonic stress regimes or fracture orientation within the reservoir for injection ($\Delta P > 0$) into the reservoir.

Direction	NF regime $S_V > S_H > S_h$ Hydraulic fractures are oriented vertical and parallel to S_H	SS regime $S_H > S_V > S_h$ Hydraulic fractures are oriented vertical and parallel to S_H	TF regime $S_H > S_h > S_V$ Hydraulic fractures are horizontal
Vertical	No change	→ NF for $\Delta P > \frac{2(S_H - S_V)}{\alpha} \cdot \frac{1-\nu}{1-2\nu}$	→ SS for $\Delta P > \frac{2(S_h - S_V)}{\alpha} \cdot \frac{1-\nu}{1-2\nu}$ and fracs vertical + parallel to S_H → NF for $\Delta P > \frac{2(S_H - S_V)}{\alpha} \cdot \frac{1-\nu}{1-2\nu}$ and fracs vertical + parallel to S_H
Along S_H	→ SS for $\Delta P > \frac{2(S_V - S_H)}{\alpha} \cdot \frac{1-\nu}{1-2\nu}$	No change	No change
Along S_h	→ SS for $\Delta P > \frac{2(S_V - S_H)}{\alpha} \cdot \frac{1-\nu}{1-2\nu}$ and the local maximum horizontal stress S_{Hl} switches to the direction of the regional S_h → fractures are parallel to regional minimum horizontal stress S_h	→ TF for $\Delta P > \frac{2(S_V - S_h)}{\alpha} \cdot \frac{1-\nu}{1-2\nu}$ and horizontal fracs → TF for $\Delta P > \frac{2(S_H - S_h)}{\alpha} \cdot \frac{1-\nu}{1-2\nu}$ and horizontal fracs and maximum horizontal stress S'_H is parallel to direction of S_h	No regime change, but for $\Delta P > \frac{2(S_H - S_h)}{\alpha} \cdot \frac{1-\nu}{1-2\nu}$ maximum horizontal stress S'_H is parallel to direction of S_h

stress is reduced by $2/3\ \Delta P$ as is the effective minimum horizontal stress, therefore the size of the blue Mohr circle remains unchanged. However at point B, the effective vertical stress and the effective maximum horizontal stress are reduced by $2/3\ \Delta P$ and the effective minimum horizontal stress, which is a radial stress, is reduced only by $1/3\ \Delta P$. This leads to decreasing differential stresses.

4.3. Strike slip regime

In a strike slip regime the differential stress is determined by S_H and S_h. During injection into a strike slip regime (e.g. the case of Basel) the differential stress increases if the S_H orientation is the radial stress (point A, blue Mohr circle); whereas if S_h is the radial stress (point B) the shear stress is decreased (red Mohr circle). Depletion in a strike slip regime causes a reduction of differential stress along the radial stress axis coinciding with the S_H orientation, and an increase along the radial stress axis in the S_h orientation.

4.4. Thrust faulting regime

In a thrust faulting regime depletion causes a reduction of the differential stress on the radial stress axis if it coincides with the S_H orientation (point A, blue Mohr circle), and an increase of differential stress at points where the S_V orientation coincides with the radial stress direction (point C, green Mohr circle). In the case of injection, the differential stress increases in the S_H orientation if it is the radial stress axis (point A, blue Mohr circle), and decreases along the radial stress axis in the S_V orientation (point C, green Mohr circle).

4.5. Changes of local stress state due to PSC and implications for the local tectonic stress regime

Since PSC affects the stress magnitudes it leads to changes in relative stress magnitudes and because the tectonic stress regime assignment is based on the relative stress magnitudes, PSC can therefore lead – on a local scale – to a change in the tectonic stress regime. The regional tectonic stress regime (normal faulting, strike slip faulting and thrust faulting) is a function of tectonic stresses on regional to global scale. However, local stress sources can change the tectonic stress regime on local scales (*Heidbach et al.*, 2007, 2010). If stress conditions prior to injection or depletion are such that two of the principal stresses are rather similar in magnitude, the tectonic stress regime can be locally changed by PSC. Such a change of tectonic stress regime (relative stress magnitudes) affects a number of geomechanical issues, such as wellbore stability, because the failure conditions around wellbores depend on the relative stress magnitudes. For example: in a normal faulting regime, wellbores drilled vertically are most stable, but in strike slip regimes vertical boreholes experience more borehole breakout formation and thus wellbore stability problems (*Fuchs and Müller*, 2001). If, during the lifetime of a producing reservoir, local variations of tectonic stress regimes are created, this can influence the planning of

Table 5
Localized change of tectonic stress regimes or fracture orientation within the reservoir for depletion ($\Delta P < 0$) into the reservoir.

Direction	NF regime $S_V > S_H > S_h$ Hydraulic fractures are oriented vertical and parallel to S_H	SS regime $S_H > S_V > S_h$ Hydraulic fractures are oriented vertical and parallel to S_H	TF regime $S_H > S_h > S_V$ Hydraulic fractures are horizontal
Vertical	→ SS for $\lvert\Delta P\rvert > \frac{2(S_V - S_H)}{\alpha} \cdot \frac{1-\nu}{1-2\nu}$ → TF for $\lvert\Delta P\rvert > \frac{2(S_V - S_h)}{\alpha} \cdot \frac{1-\nu}{1-2\nu}$ and horizontal fracs	→ TF for $\lvert\Delta P\rvert > \frac{2(S_V - S_h)}{\alpha} \cdot \frac{1-\nu}{1-2\nu}$ and horizontal fracs	No change
Along S_H	for $\lvert\Delta P\rvert > \frac{2(S_H - S_h)}{\alpha} \cdot \frac{1-\nu}{1-2\nu}$ the maximum horizontal stress S_{Hl} switches to direction of the regional S_h → vertical fractures are now parallel to original minimum horizontal stress S_h	→ NF for $\lvert\Delta P\rvert > \frac{2(S_H - S_V)}{\alpha} \cdot \frac{1-\nu}{1-2\nu}$ → TF for $\lvert\Delta P\rvert > \frac{2(S_H - S_h)}{\alpha} \cdot \frac{1-\nu}{1-2\nu}$ and maximum horizontal stress S_{Hl} switches to direction of the regional S_h → vertical fractures are now parallel to original minimum horizontal stress S_h	for $\lvert\Delta P\rvert > \frac{2(S_H - S_h)}{\alpha} \cdot \frac{1-\nu}{1-2\nu}$ the maximum horizontal stress S_{Hl} switches to direction of S_h → SS $\lvert\Delta P\rvert > \frac{2(S_H - S_V)}{\alpha} \cdot \frac{1-\nu}{1-2\nu}$ for → vertical fracs parallel to S_H
Along S_h	No change	No change	→ SS for → vertical fracs parallel to S_H

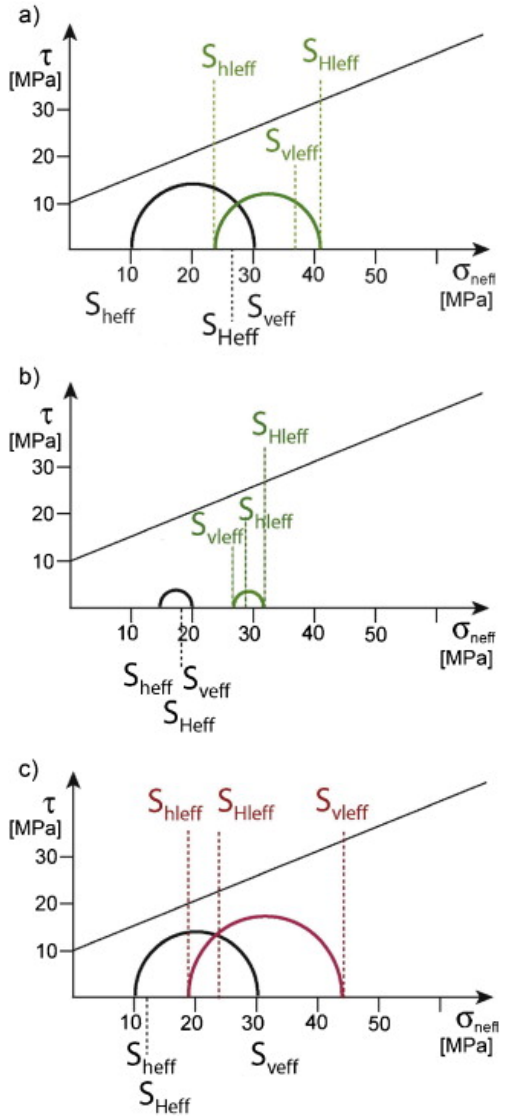

Figure 6. Examples of stress regime change caused by production-induced changes of the stress components in an initially normal faulting stress regime (black circles) and changes due to reduction of pore pressure by $P = 21$ MPa (green and red circles). (a) $S_{V_{eff}}$ = 30 MPa > $S_{H_{eff}}$= 27 MPa > $S_{h_{eff}}$ = 10 MPa: along a vertical trace above or below the production interval, the local effective stress state is $S_{Hl_{eff}}$ = 41 MPa, $S_{Vl_{eff}}$ = 37 MPa, $S_{hl_{eff}}$ = 24 MPa. This means that there is a local change in tectonic stress regime from originally normal faulting to strike slip. (b) For a more isotropic initial state $S_{V_{eff}}$ = 20 MPa > $S_{H_{eff}}$ = 18 MPa > $S_{h_{eff}}$ = 15 MPa the $P = 21$ MPa leads locally to a thrust faulting regime with ($S_{Hl_{eff}}$ = 32 MPa > $S_{hl_{eff}}$ = 29 MPa > $S_{Vl_{eff}}$= 27 MPa). In this case stimulation fractures would initiate as horizontal fractures instead of vertical fractures as would be expected in the regional normal faulting regime. (c) Along a horizontal trace parallel S_H with the regional stress $S_{V_{eff}}$ = 30 MPa > $S_{H_{eff}}$ = 12 MPa > $S_{h_{eff}}$ = 10 MPa, a reduction of $P = 21$ MPa increases $S_{V_{eff}}$ and $S_{h_{eff}}$ by 14 MPa whereas the increase of $S_{H_{eff}}$ is only 7 MPa. This leads to a switch in the orientation of horizontal stresses so that stimulation fractures would be parallel to the local S_h orientation which is perpendicular to the S_H orientation: $S_{Vl_{eff}}$ = 44 MPa > $S_{Hl_{eff}}$ = 24 MPa > $S_{hl_{eff}}$ = 19 MPa. (For interpretation of the references to colour in this figure legend, the reader is referred to the web version of the article.)

infill wells. Furthermore, the orientation of hydraulically induced fractures might change due to local stress regime modification. For example in strike slip regimes the fractures are vertical, perpendicular to the S_h orientation; in a thrust faulting regime the fractures might be horizontal because the least principal stress is S_V (Tables 4 and 5).

Fig. 6 illustrates the consequences for an (initially): normal faulting regime, with similar values of the effective minimum horizontal and vertical stresses ($\Delta S_{V_{eff}}$ = 30 MPa > $\Delta S_{H_{eff}}$ = 27 MPa > $\Delta S_{h_{eff}}$ = 10 MPa). During reduction of pore pressure by $P = 21$ MPa, the effective stresses along a vertical trace above or below the production interval change locally to $\Delta S_{H_{eff}}$ = 41 MPa, $\Delta S_{V_{eff}}$ = 37 MPa, $\Delta S_{h_{eff}}$ = 24 MPa (Fig. 6a). This means that there is a local change in tectonic stress regime from normal faulting to strike slip. If the initial state of stress is close to isotropic (Fig. 6b, $\Delta S_{V_{eff}}$ = 20 MPa > $\Delta S_{H_{eff}}$ = 18 MPa > $\Delta S_{h_{eff}}$ = 15 MPa) the same pore pressure reduction would locally lead to a thrust faulting regime with ($\Delta S_{Hl_{eff}}$ = 32 MPa > $\Delta S_{hl_{eff}}$ = 29 MPa > $\Delta S_{Vl_{eff}}$ = 27 MPa). In this case stimulated fractures would initiate as horizontal rather than vertical fractures as would be expected in the regional normal faulting regime. Fig. 6c illustrates the state of stress along a horizontal trace parallel to the S_H orientation when the initial stress is described by $S_{V_{eff}}$ = 30 MPa > $S_{H_{eff}}$ = 12 MPa > $S_{h_{eff}}$ = 10 MPa. The same pore pressure reduction increases $S_{V_{eff}}$ and $S_{h_{eff}}$ by 14 MPa whereas the increase of $S_{H_{eff}}$ is only 7 MPa. This leads to a switch in the orientation of horizontal stresses so that stimulation fractures would be parallel to the local maximum horizontal stress, which is perpendicular to the regional maximum horizontal stress: $S_{Vl_{eff}}$ = 44 MPa > $S_{Hl_{eff}}$ = 24 MPa > $S_{hl_{eff}}$ = 19 MPa.

The modification of tectonic stress regimes can also be described as a function of pore pressure change and initial relative stress states. Under standard assumptions for Poisson's ratio ($\nu = 0.25$ and Biot–Willis coefficient $\alpha = 1$) a regime change is most probable if the change in pore pressure exceeds ca. three times the maximum initial differential stress, because the equations of Tables 2 and 3 can be approximated by

$$|\Delta P| > \frac{2(S_H - S_h)}{\alpha}\frac{1-2}{1-2\nu} \cong 3(S_H - S_h) \qquad (13)$$

Our findings are based on analytical solutions by *Rudnicki* (1986) which represent point injection/depletion into a homogeneous full space. They will not apply for realistic reservoir geometries, but they can help to interpret the results of numerical modelling for detailed reservoir geometries. Reservoir compaction as well as related deformations and displacements from

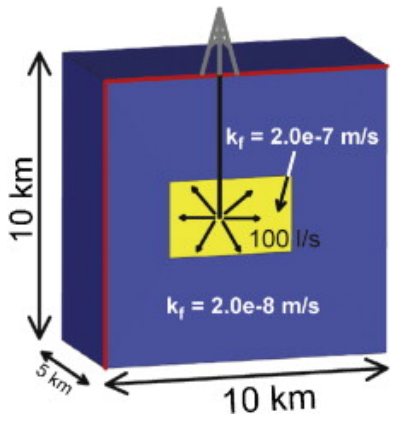

Figure 7. Geomechanical-numerical model of an artificial reservoir in a normal faulting regime ($S_1 = S_V$, $S_2 = S_H$, $S_3 = S_h$) for two years of production with a production rate of 100 l/s.

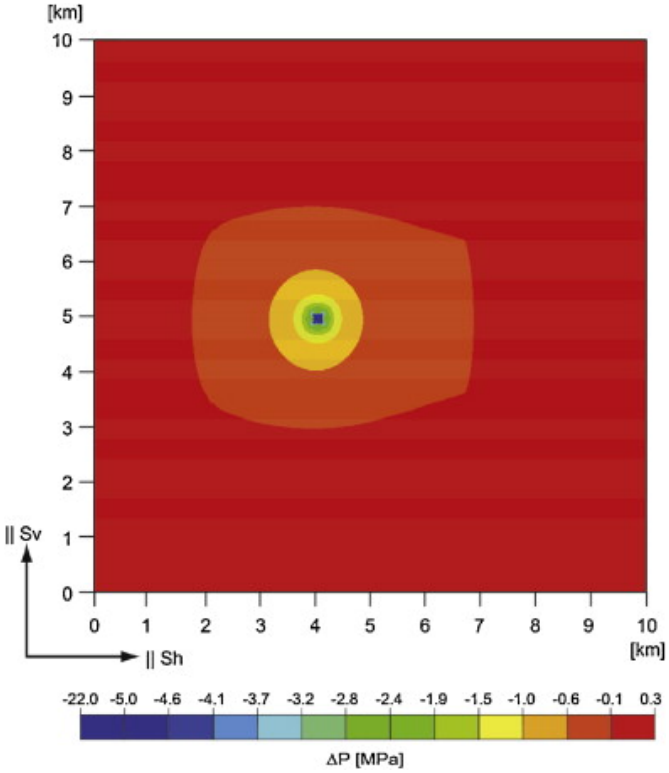

Figure 8. Simulated changes of pore pressure for a reservoir in a normal faulting stress regime ($S_1 = S_V$, $S_2 = S_H$, $S_3 = S_h$) after 2 years of production from a single point. The vertical cross section is a plane through the well which is oriented perpendicular to S_H.

more realistic reservoirs have to be studied by 3D numerical modelling (*Schutjens et al.*, 2010; *Rutqvist et al.*, 2013). In the following section we present a generic 3D geomechanical-numerical model of the poro-elastic equations for a point source in a reservoir with inhomogeneous rock properties.

5. Geomechanical-numerical modelling

In contrast to the solutions above, real production and reinjection scenarios are often quite complex. Furthermore, rock properties are neither isotropic nor homogeneous and thus geomechanical-numerical models are compulsory to investigate the spatio-temporal evolution state of stress during the lifetime of a reservoir. However, our analytical results can be important to interpret the results of geomechanical-numerical modelling as shown in the example below.

Fig. 7 illustrates a numerical model of an artificial reservoir in a normal faulting regime ($S_1 = S_V$, $S_2 = S_H$, $S_3 = S_h$) with a production rate of 100 l/s. The reservoir is simplified as a cube with a permeability of 2.0×10^{-14} m^2 embedded in a surrounding with a significantly reduced permeability of 2.0×10^{-15} m^2. The model sides and bottom are fixed in normal direction and the surface is freely moving. The initial pore pressure distribution is hydrostatic.

Fig. 8 shows the results in terms of changes in pore pressure and in maximum differential stresses after two years of production. The results of the numerical modelling complement the previous analytical results: in the immediate vicinity of the production well, pore pressure changes are on the order of 20 MPa; they reduce to less than 1 MPa at greater distances (Fig. 8). Fig. 9 shows the corresponding poro-elastic changes of the maximum shear distributions, which demonstrate the anisotropy in shear stress changes: the maximum shear stress is reduced above and below the production point, no changes occur at positions along the x-axis (which is parallel to the S_H orientation), and the maximum increase in shear stress occurs parallel to the y-axis, which is parallel to the S_h orientation. The shear stress changes for this model are in the order of 0.2 MPa and would seem to be rather small. However, if we consider a longer time interval such as 10 years of production (or even a number of production wells in close vicinity) the change in pore pressure could increase to about 10 MPa, and the corresponding shear stress changes of individual wells would be on the order of 2 MPa. Since this solution is a poro-elastic solution, the results of individual wells can be superimposed, perhaps leading to significant shear stress changes.

6. Practical implications for reservoir stability and management

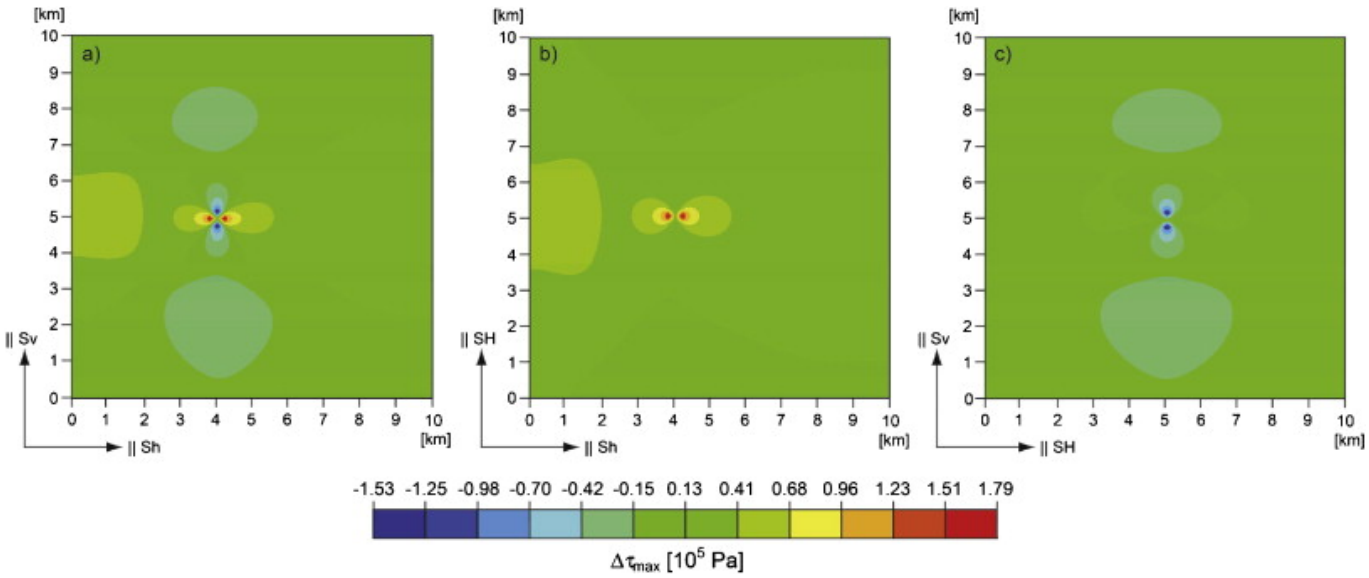

Figure 9. Simulated changes of maximum shear stress for a reservoir in a normal faulting stress regime ($S_1 = S_V$, $S_2 = S_H$, $S_3 = S_h$) after 2 years of production from a single point. The cross sections are perpendicular to (a) S_H, (b) S_V and (c) S_h.

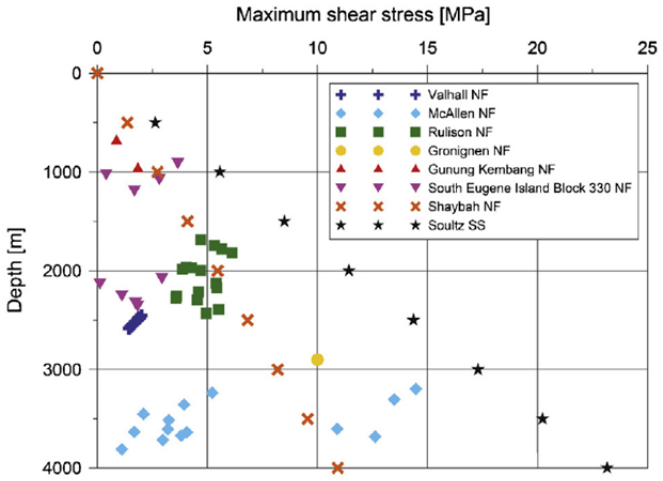

Figure 10. Maximum shear stresses within reservoirs versus depth: Valhall, McAllen, Rulison (*Teufel et al.*, 1991), Groningen (*Hettema et al.*, 1998), Shaybah (*Salamy and Finkbeiner*, 2002), Gunung Kembang (*Dwi Hudya et al.*, 2007), Eugene Island Block 330 (*Finkbeiner and Zoback*, 1998).

6.1. Fault reactivation

Because the level of shear stress is critical for fault reactivation, fault reactivation is more likely for faults in high shear stress regions. Increasing shear stress destabilizes pre-existing faults, whereas decreasing shear stress leads to stabilization (Fig. 5). PSC results in spatial variations of shear stress changes. Therefore, some faults will be closer to reactivation than others, depending on their position with respect to the injection/depletion point. During injection into a strike slip regime (e.g. case of Basel) the differential stress increases in the orientation of the maximum horizontal stress (point A, blue Mohr circle, Fig. 5), which brings pre/existing faults located along this orientation closer to failure, whereas faults located along the minimum horizontal stress (point B, Fig. 5) can even be stabilized (red Mohr circle). Reactivation in the case of injection into a normal faulting regime is most likely on faults located parallel to S_V, i.e. above and below the injection point.

6.2. Well stability

Changes in total stress magnitudes resulting from PSC have direct implications for the stability of infill wells drilled close to previously producing wells. Drillers estimate mud weights to stay in the so-called drilling window, which is a pressure range roughly between the formation pore pressure and the tangential stress concentrations, which are direct functions of the local stress state at the borehole wall. Control of drilling mud weight is necessary to avoid wellbore collapse or uncontrolled formation fluid influx. When the mud pressure is too high, compared to the tangential stress concentrations at the wellbore wall, unwanted fracturing of the formation can lead to total loss of drilling fluid. This occurs at the upper end of the drilling window, which is defined by the fracture pressure at which the drilling fluid pressure exceeds the tangential stress at the borehole wall and creates a hydraulic fracture. Our analysis suggests that predrilling wellbore stability predictions have to take into account the effect of PSC, especially when additional wells are drilled into formations that had experienced a significant pore pressure reduction.

Production induced poro-elastic stress changes can lead to changes in shear stress on the order of a few MPa up to several 10 s of MPa in very deep reservoirs that are producing for a long period (*Segall et al.*, 1994). Furthermore, during fluid injection under high pressure e.g. for stimulation, the stresses in the near-field will change significantly and lead to stress rotation as shown for The Geysers geothermal field (*Martínez-Garzón et al.*, 2013). These changes do not affect the maximum shear stress pattern significantly in cases where the differential stresses or shear stresses are already large, e.g. $S_V \gg S_H \gg S_h$ in case of normal faulting at greater depth, or $S_H \gg S_V \gg S_h$ in the case of strike slip regimes. However, for shallow depths, such as reservoirs at 1–3 km depth, total stresses and the difference in horizontal stress are rather small (Fig. 10). The effect of PSC therefore is expected to be more significant for shallower reservoirs, in areas with low shear stress, and in reservoirs where significant changes in pore pressure will occur during depletion.

7. Conclusion

Pore pressure/stress coupling (PSC) has a tensor character and can cause significant changes in the stress field. We analyse the impact of pore pressure changes on all components of the stress tensor. Our results show:

(1) Pore pressure affects not only S_h magnitudes but also the other stress components. The absolute changes of tensor components are directly related to the change in pore pressure. The stress changes can be a significant fraction of pore pressure changes (often 60–80% of the pressure change).
(2) In our spherical symmetrical example the stress components from PSC can be considered in terms of radial and tangential stresses with respect to the pore pressure cloud. In the long-term limit of production pore pressure induced stress changes of the radial stress components are twice as large as the change of the tangential stress components.
(3) The stresses induced by pore pressure changes modify the likelihood of reactivation of faults. During injection in strike slip and thrust faulting stress regimes, the likelihood for fault reactivation is greatest along the S_H orientation, whereas in normal faulting stress regimes reactivation is most likely above or below the injection point along the S_V orientation.
(4) During depletion in normal faulting and strike slip stress regimes fault reactivation is most likely in the S_h orientation. In a thrust faulting stress regime reactivation is most likely in the S_V orientation.
(5) PSC can locally modify the relative stress magnitudes. This is a function of pore pressure change and the initial relative stress state. This is most likely if the change in pore pressure exceeds three times the maximum initial shear stress.
(6) The effects of PSC on stress magnitudes are especially important in reservoirs that experienced significant pressure changes e.g. due to high injection and production rates.

The integrity of reservoirs depends on the seal capacity of the cap rock layers (normally silt and shale) and of the reservoir bounding faults (*Sneider and Sneider*, 2002). If these seals break due to changes in stress and pressure, the structure of the reservoir are significantly disturbed. Our investigations contribute to the understanding of the spatial and temporal dependence of potential seal or cap rock leakage, injection and depletion related seismicity in reservoirs, effectiveness of secondary production methods, and stability of infill wells as a consequence of reservoir injection and depletion from the reservoir. The effects of PSC on stress magnitudes and tectonic stress regimes should be taken into account in planning additional wells for secondary or tertiary production measures. Furthermore, the PSC methodology should be considered for the early times of injection when

the variations of stress and pore pressure (Fig. 3) can lead to considerable variations of effective stress with time.

Acknowledgements

The work presented was funded by the Department of Energy Geothermal Technologies Program under Award Number DE-EE0002756-002, the European Commission within the FP7 project GEISER, grant agreement no. 241321 and by the sponsors of the consortium project PHASE at the FU Berlin. We thank the Ministry for Science, Research and Arts of Baden-Württemberg for funding the LFZG. We thank Peter Schutjens for a number of very constructive comments on an earlier version of the manuscript. We also thank Jonny Rutqvist and Steve Ingebritsen for the very constructive comments and suggestions that improved our paper.

References

Addis, M.A., 1997. The Stress-Depletion Response of Reservoirs Paper Presented at SPE 38720 , San Antonio, TX, 5–8 October.

Altmann, J., Müller, T., Müller, B., Tingay, M., Heidbach, O., 2010. Poroelastic contribution to the reservoir stress path. International Journal of Rock Mechanics and Mining Science 47, 1104–1113, http://dx.doi.org/10.1016/j.ijrmms.2010.1108.1001.

Biot, M.A., 1962. Mechanics of deformation and acoustic propagation in porous media. Journal of Applied Physics 33 (4), 1482–1498.

Bishop, A.W., 1959. The Principle of Effective Stress, vol. 39. Teknisk, UK, pp. 859–863.

Braun, R., 2007. A commonly neglected factor in rock mass and borehole stability. OIL GAS European Magazine 2, OG79–OG82.

Coulomb, C.A., 1773. Application des règles de maxima et minima à quelques problèmes de statique relatifs à l'Architecture. Mémoires de Mathématique et de Physique, vol. 7. Académie Royale des Sciences par divers sans., pp. 343–382.

Cuenot, N., Charléty, J., Dorbath, L., Haessler, 2006. Faulting mechanisms and stress regime at the European HDR site of Soultz-sous-Forêts, France. Geothermics 35, 561–575.

Deichmann, N., Evans, K., 2007. Seismicity induced by water injection for geothermal reservoir stimulation 5 km below the city of Basel, Switzerland. In: Paper presented at AGU Fall Meeting.

Dwi Hudya, F., Natalia, S., Castillo, D.A.,2007. The effect of pressure depletion on geomechanical stress and fracture behaviour in Gunung Kembang Field. In: Paper presented at Thirty-First Annual Convention and Exhibition. Indonesian Petroleum Association.

Engelder, T., Fischer, M.P., 1994. Influence of poroelastic behavior on the magnitude of minimum horizontal stress, S h , in overpressured parts of sedimentary basins. Geology 22, 949–952.

Evans, K.F., Zappone, A., Kraft, T., Deichmann, N., Moia, F., 2012. A survey of the induced seismic response to fluid injection in geothermal and CO2 reservoirs in Europe. Geothermics 41, 1030–1054, http://dx.doi.org/10.1016/j.geothermics.2011.1008.1002.

Finkbeiner, T., Zoback, M., 1998. Characterization of the Full Stress Tensor in Eugene Island Block 330, Offshore Gulf of Mexico, vol. 3. Gas Research Institute.

Fuchs, K., Müller, B., 2001. World Stress Map of the Earth: a key to tectonic processes and technological applications. Naturwissenschaften 88 (9), 357–371.

Goulty, N.R., 2003. Reservoir stress path during depletion of Norwegian chalk oilfields. Petroleum Geosciences 9, 233–241.

Goyal, K.P., Conant, T.T., 2010. Performance history of The Geysers steam field, CA, USA. Geothermics 39 (4), 321–328, http://dx.doi.org/10.1016/j.geothermics.2010.1009.1007.

Grasso, J.R., Wittlinger, G., 1990. Ten years of seismic monitoring over a gas field. Bulletin of the Seismological Society of America 80 (2), 450–473.

Heidbach, O., Reinecker, J., Tingay, M., Müller, B., Sperner, B., Fuchs, K., Wenzel, F., 2007. Plate boundary forces are not enough: second- and third-order stress patterns highlighted in the World Stress Map database. Tectonics 26, TC6014, http://dx.doi.org/10.1029/2007TC002133.

Heidbach, O., Tingay, M., Barth, A., Reinecker, J., Kurfeß, D., Müller, B., 2010. Global crustal stress pattern based on the World Stress Map database release 2008. Tectonophysics 482 (1–4), 3–15, http://dx.doi.org/10.1016/j.tecto.2009.07.023.

Herwanger, J., Horne, S., 2005. Predicting time-lapse stress effects in seismic data. The Leading Edge 24 (12), 1234–1241.

Hettema, M.H.H., Schutjens, P.M.T.M., Verboom, B.J.M., Gussinklo, H.J., 1998. Production – induced compaction of sandstone reservoirs: the strong influence of field stress. In: Society of Petroleum Engineers European Petroleum Conference, The Hague.

Hillis, R.R., 2000. Pore pressure/stress coupling and its implications for seismicity. Exploration Geophysics 31, 448–454.

Hillis, R.R., 2001. Coupled changes in pore pressure and stress in oil fields and sedimentary basins. Petroleum Geoscience 7, 419–425.

Jaeger, J.C., Cook, N.G.W., Zimmerman, R.W., 2007. Fundamentals of Rock Mechanics. Blackwell, 475 pp.

Majer, E.L., Baria, R., Stark, M., Oates, S., Bommer, J., Smith, B., Asanuma, H., 2007. Induced seismicity associated with enhanced geothermal systems. Geothermics 36, 185–222.

Martínez-Garzón, P., Bohnhoff, M., Kwiatek und, G., Dresen, G., 2013. Stress tensor changes relate to fluid injection at The Geysers geothermal field, California. Geophysical Research Letters 118 (1–6), http://dx.doi.org/10.1001/grl.50438.

Maxwell, S.C., Urbancic, T.I., 2001. The role of passive microseismic monitoring in the instrumented oil field. The Leading Edge 20, 636–639.

Mossop, A.P., Segall, P., 1997. Subsidence at The Geysers geothermal field, N. California from a comparison of GPS and leveling surveys. Geophysical Research Letters 24, 1839–1842.

Pennington, W.D., Davis, S.D., Carlson, S.M., DuPree, J., Ewing, T.E., 1986. The evolution of seismic barriers and asperities caused by the depresuring of fault planes in oil and gas fields of South Texas. Bulletin of the Seismological Society of America 76 (4), 939–948.

Rozhko, A.Y., 2010. Scaling of fluid-induced seismicity by Coulomb stress transfer model. In: Paper Presented at 72nd EAGE Conference & Exhibition, EAGE, Barcelona, 14–17 June.

Rudnicki, J.W., 1986. Fluid mass sources and point forces in linear elastic diffusive solids. Mechanics of Materials 5, 383–393.

Rutqvist, J., Birkholzer, J.T., Tsang, C.-F., 2008. Coupled reservoir-geomechanical analysis of the potential for tensile and shear failure associated with CO_2 injection in multilayered reservoir-caprock systems. International Journal of Rock Mechanics and Mining Science 45, 132–143.

Rutqvist, J., Dobson, P.F., Garcia, J., Hartline, C., Oldenburg, C.M., Vasco, D.W., Walters, M., 2013. Pre-stimulation coupled THM modeling related to the Northwest Geysers EGS Demonstration Project. In: Proceedings of the 38th Workshop on Geothermal Reservoir Engineering, Stanford, CA, 11–13 February, 2013.

Salamy, S.P., Finkbeiner, T., 2002. A poroelastic analysis to address the impact of depletion rate on wellbore stability in openhole horizontal completions. In: Paper Presented at 10th Abu Dhabi International Petroleum Exhibition and Conference ADIPEC, Abu Dhabi, 13–16 October.

Sarker, R., Batzle, M., 2008. Effective stress coefficient in shales and its applicability to Eaton' equation. The Leading Edge 27, 798–804, http://dx.doi.org/10.1190/1.2944165.

Sayers, C., 2004. Inversion of elastic wave velocity measurements for monitoring changes in rock stress resulting from production. In: Paper presented at Gulf Rocks 2004. The 6th North America Rock Mechanics Symposium, NARMS, Houston, TX, 5–9 June.

Sayers, C., 2006. Sensitivity of time-lapse seismic to reservoir stress path. Geophysical Prospecting 54, 369–380.

Schoenball, M., Müller, T.M., Müller, B.I.R., Heidbach, O., 2010. Fluid-induced microseismicity in pre-stressed rock masses. Geophysical Journal International 180(2), 813–819.

Schutjens, P.M.T.M., Snippe, J.R., Mahani, H., Turner, J., Ita, J., Mossop, A.P., 2010. Production-induced stress change in and above a reservoir pierced by two salt domes: a geomechanical model and its applications. In: Paper presented at SPE EUROPEC/EAGE Annual Conference and Exhibition EAGE, Barcelona, Spain.

Segall, P., 1992. Induced stresses due to fluid extraction from axisymmetric reservoirs. Pure and Applied Geophysics 139, 535–560.

Segall, P., Fitzgerald, S.D., 1998. A note on induced stress changes in hydrocarbon and geothermal reservoirs. Tectonophysics 289, 117–128.

Segall, P., Grasso, J.-R., Mossop, A., 1994. Poroelastic stressing and induced seismicity near the Lacq gas field, southwestern France. Journal of Geophysical Research 99 (B8), 15423–15438.

Settari, A., Sen, V., 2007. The role of geomechanics in integrated reservoir modelling. The Leading Edge 26, 622–627, http://dx.doi.org/10.1190/1.2737102.

Shapiro, S.A., Royer, J.-J., Audigane, P., 1998. Estimating the permeability from fluid-injection induced seismic emission. In: Thimus, J.-F. (Ed.), Poromechanics. A Tribute to Maurice A. Biot. Balkema, Leiden, The Netherlands, pp. 301–305.

Shapiro, S.A., Patzig, R., Rothert, E., Rindschwentner, J., 2003. Triggering of seismicity by pore-pressure perturbations: permeability-related signatures of the phenomenon. Pure and Applied Geophysics 160 (5/6), 1051–1066.

Sneider, R.M., Sneider, J.S., 2002. Importance of Seals and Flow Barriers in E&P Projects. In: AAPG Hedberg Research Conference Evaluating the Hydrocarbon Sealing Potential of Faults and Caprocks, Barossa Valley, South Australia, pp. 10–13.

Suckale, J., 2010. Moderate-to-large seismicity induced by hydrocarbon production. The Leading Edge 29, 310–319, http://dx.doi.org/10.1190/1.3353728.

Terzaghi, K., 1943. Theoretical Soil Mechanics. Wiley and Sons, New York, pp. 510.

Teufel, L.W., Rhett, D.W., Farrell, H., 1991. Effect of reservoir depletion and pore pressure drawdown on in situ stress and deformation in the Ekofisk field, North Sea. In: Rogiers, J.-C. (Ed.), Rock Mechanics as a Multidisciplinary Science: Proceedings of the 32nd Symposium on Rock Mechanics, Balkema, Rotterdam, pp. 63–72.

Tingay, M., Hillis, R.R., Morley, C.K., Swarbrick, E., Okpere, E.C., 2003. Pore pressure/stress coupling in Brunei Darussalam – implications for shale injection. In: van Rensbergen, P., Hillis, R.R., Maltman, A.J., Morley, C.K. (Eds.), Morley Subsurface Sediment Mobilization. Geological Society, London, pp. 369–379.

Valley, B., Evans, K., 2007. Stress state at Soultz-sous-Forêts to 5 km depth from well-bore failure and hydraulic observations. In: Paper Presented at Thirty-Second Workshop on Geothermal Reservoir Engineering Stanford University, Stanford, California, 22–24 January.

Wang, H.F., 2000. Theory of Linear Poroelasticity. Princeton University Press, Prince-ton, New Jersey, USA, pp. 287.

Zoback, M.D., 2010. Reservoir Geomechanics, 2nd ed., Cambridge University Press, Cambridge, 449 pp.